Optical-Model Analysis with Spin-Orbit Potential for 30- and 35-MeV ^{3}He Elastic Scattering*

J. W. LUETZELSCHWAB† AND J. C. HAFELE

Department of Physics, Washington University, Saint Louis, Missouri 63130

(Received 26 December 1968)

Measured differential cross sections are reported for 30-MeV ^{3}He ions elastically scattered from ^{27}Al, ^{51}V, ^{59}Co, ^{60}Ni, ^{89}Y, ^{114}Cd, ^{115}In, and ^{116}Sn for angles between 6° and 165° and for 35-MeV ^{3}He ions elastically scattered from ^{59}Co, ^{60}Ni, ^{115}In, and ^{116}Sn for angles between 6° and 140°. The data are compared with predictions of the nuclear optical model, and potential parameters that produce optimum fits with a least-squares computer routine are reported. Good fits at back angles for ^{27}Al, ^{51}V, ^{59}Co, and ^{60}Ni are obtained only with the inclusion of a spin-orbit interaction with a magnitude between 2 and 5 MeV for most cases. The back-angle data for these nuclei also tend to suppress discrete ambiguities in the potential well depths. A continuous ambiguity between the radius and the diffuseness parameters is found to be related to a constancy of the root-mean-square radius. Effects of experimental uncertainties on the potential parameters are also presented.

I. INTRODUCTION

FOR many years the optical model has been used successfully to fit ^{3}He elastic scattering data, and optical-potential parameters have been obtained for several energies over a wide range of targets.[1–4] Nevertheless, the potential wells remain rather poorly defined mainly because of disturbing ambiguities,[5] both discrete and continuous, that arise in the determination of the parameters. Ambiguities exist between discrete sets or families of parameters and, within a given family, between well depth and radius parameters and between radius and diffuseness parameters.

Regardless of the observational ambiguities, it is theoretically expected[6] that, for loosely bound projectiles such as deuterons, tritons, or ^{3}He ions, the depth of the real potential well should be approximately the number of nucleons comprising the projectile times the depth (~50 MeV) for single nucleons, or about 150 MeV for ^{3}He projectiles. In most previous investigations of ^{3}He scattering, however, shallower wells (~50 MeV) were found to produce good fits to the data,[1] though subsequent studies[3,7,8] have shown that equally good fits could have been obtained with a depth of about 150 MeV. The results of one recent investigation[3] show that, though parameter families with different real depths give equally good fits to the data recorded in this case for angles less than 90°, the optical-model predictions differ greatly for larger angles. This difference suggests that back-angle data may give an experimental basis for choosing a preferred real well depth.

The glaring lack in the literature of back-angle data for ^{3}He elastic scattering is understandable; the differential cross sections in this region are quite small and the experiments are time-consuming. Nevertheless, back-angle data may reveal a wealth of information about fine effects that occur in the fundamental projectile-nucleus interaction. For example, the effects that spins (both target and projectile) have on the ^{3}He differential cross sections is still largely unknown. It has been known for some time that a spin-orbit interaction is necessary to explain the scattering and polarization data for protons and neutrons, and the spin-orbit depth in this case has been found to lie between 5 and 10 MeV for low to medium energies.[1,9,10] A similar spin-orbit interaction should also occur for compound projectiles with spin. Although there is little relevant data for ^{3}He projectiles,[11–13] the depth of the spin-orbit inter-

* Accelerator time for this research was supported by the U.S. Atomic Energy Commission Grant No. AT(11-1)-1760. Computer time was furnished by the Washington University Computing Facilities (National Science Foundation Grant No. G-22296). This article is based on a doctoral dissertation submitted by one of the authors (JWL) to the faculty of Washington University.

† Present address: Dickinson College, Carlisle, Pa.

[1] P. E. Hodgson, *The Optical Model of Elastic Scattering* (Oxford University Press, London, 1963).

[2] R. H. Siemssen, T. H. Braid, D. Dehnard, and B. Zeidman, Phys. Letters **18**, 155 (1965); D. J. Baugh, G. J. B. Pyle, P. M. Rolph, and S. M. Scarrott, Nucl. Phys. **A95**, 115 (1967); R. J. Griffiths, *ibid.* **A102**, 329 (1967); C. R. Bingham and M. L. Halbert, Phys. Rev. **158**, 1085 (1967).

[3] E. F. Gibson, B. W. Ridley, J. J. Kraushaar, M. E. Rickey, and R. H. Bassel, Phys. Rev. **155**, 1194 (1967).

[4] C. R. Bingham and M. L. Halbert, Phys. Rev. **169**, 933 (1968).

[5] R. M. Drisko, G. R. Satchler, and R. H. Bassel, Phys. Letters **5**, 347 (1963).

[6] S. Watanabe, Nucl. Phys. **8**, 484 (1958); J. R. Rook, *ibid.* **61**, 219 (1965); J. Schiffer, Brookhaven National Laboratory Report No. BNL 948 (C-46), 1965, Vol. II, p. 455 (unpublished).

[7] D. E. Rundquist, M. K. Brussel, and A. I. Yavin, Phys. Rev. **168**, 1287 (1968).

[8] H. T. Fortune, T. J. Gray, W. Trost, and N. R. Fletcher, Phys. Rev. **173**, 1002 (1968).

[9] Spin-orbit potentials appearing in the literature are defined in several different ways. The magnitudes given here are consistent with the spin-orbit potential defined later.

[10] G. W. Greenlees and G. J. Pyle, Phys. Rev. **149**, 836 (1966); F. Bjorklund and S. Fernbach, *ibid.* **109**, 1295 (1958).

[11] Recently reported results for ^{3}He scattering from ^{12}C (Refs. 12 and 13) are consistent with a spin-orbit potential depth inversely proportional to the atomic mass of the projectile.

[12] D. M. Patterson and J. G. Cramer, Phys. Letters **27B**, 373 (1968).

[13] R. L. Hutson, S. Hayakawa, M. Chabre, J. J. Kraushaar, B. W. Ridley, and E. T. Boschitz, Phys. Letters **27B**, 153 (1968).

action in this case is expected theoretically[4] to be only about one-third that for single nucleons, or about 2–3 MeV. Significant effects of the spin-orbit interaction on elastic scattering are known to occur, if at all, only at back angles; thus back-angle data may throw additional light on the effect and magnitude of the spin-orbit interaction.

Back-angle data requiring the spin-orbit interaction probably would have another important consequence. A study[14] of deuteron scattering has shown that the family of parameters with a real well depth of about 100 MeV (2×50 MeV) is preferred in the fitting procedure when the spin-orbit potential is included, whereas there is no preference between parameter families without a spin-orbit term. Similarly, acquisition of ^{3}He scattering data that require the inclusion of a spin-orbit interaction for good fits also may help in choosing a preferred real depth solely on an observational basis.

Rather little is known about target spin effects. For 3- to 20-MeV α particles incident on ^{9}Be (target spin $I=\frac{3}{2}$), the potential depth of the interaction of the target spin with its orbital angular momentum (in the barycentric system) has been found to be about 2 MeV.[15] However, the strength of this "inverse" or "target" spin-orbit potential is expected to be inversely proportional to the atomic mass of the target,[1] so that for ^{3}He scattering from ^{59}Co($I=\frac{7}{2}$) the magnitude of this potential, being proportional to I, should be less than about 0.7 MeV. Though this strength is considerably less than the expected strength of the "direct" spin-orbit interaction (2–3 MeV), effects depending on this target spin-orbit interaction may be strong enough to appear in back-angle data for certain odd-A nuclei under favorable circumstances. The major effect that is expected on the basis of several theoretical studies[16] is a damping of the undulations in the back-angle region for targets with nonzero spin compared with the back-angle undulations for neighboring spinless targets.

Effects of the target-spin–projectile-spin interaction are expected to be quite weak and have not been observed for compound projectiles; the strength of this interaction has been predicted to be less than about 0.1 MeV.[17]

This paper gives the results of a study of elastic scattering of 30-MeV ^{3}He projectiles from nine targets over an angular range of 6°–165°, and 35-MeV ^{3}He projectiles from four targets over an angular range of 6°–140°. Emphasis was placed on the acquisition of back-angle data for two reasons: (i) to try to observe effects on elastic scattering from the spin-orbit potential and perhaps also estimate its magnitude, and (ii) to try observationally to determine preferred real well depths. We have been definitely successful in showing that in certain cases the back-angle fits are quite unreasonable without the inclusion of the spin-orbit potential (but very good with it) and have been partially successful in estimating its magnitude in those cases. Moreover, since target spin interactions of sufficient strength are expected to damp back-angle undulations, any relative damping appearing in the comparison of the angular distributions of ^{59}Co with those of ^{60}Ni might be interpreted as arising from the nuclear spin of ^{59}Co, and there is some evidence that the back-angle undulations for these two targets are different.

Finally, the parameters of the optical potential are likely to be ill defined not only because of ambiguities in the potential but also because of systematic uncertainties in the data. Random errors in the data, such as those arising from the statistics of a finite count, do not contribute significantly to parameter uncertainties because they tend to cancel out over the entire angular distribution; but systematic errors, such as those in the measurements of angles, projectile energies, and thickness of targets, cause systematic differences in the parameters.[18] The effects that such systematic errors have on our potential parameters will be discussed.

II. EXPERIMENTAL METHOD

The Washington University variable-energy Cyclotron was used to accelerate the ^{3}He-ion beams used in this experiment to about 30 and 35 MeV. The target under study was positioned at the center of a 1.1-m-diam scattering chamber with a remotely controlled, multitarget mount.[19] A collimating slit located 25 cm upstream from the target defined the position of the beam spot at the target and limited its diameter to less than 3 mm. The unscattered beam was collected in a Faraday cup 3.3-m long and intergrated to within ±1% with the aid of a current-to-frequency converter.[20]

The 30° bend of a beam switching magnet was used to momentum-analyze the beam and thereby determine its energy to within ±1%.[19] Initially the magnet was calibrated by determining the energies of proton, α, and ^{3}He beams using the crossover method of Bardin and Rickey[21] and of Smythe.[22] Generally, the beam energy spread was about 200 keV.

The scattered particles were detected with an appropriate ΔE-E' combination of silicon surface-

[14] C. M. Perey and F. G. Perey, Phys. Rev. **152**, 923 (1966).
[15] R. B. Taylor, N. R. Fletcher, and R. H. Davis, Nucl. Phys. **65**, 318 (1965).
[16] H. C. Bryant and N. Jarmie, Ann. Phys. (N.Y.) **47**, 127 (1968); R. Ceuleneer, M. Demeur, and J. Reignier, Nucl. Phys. **89**, 177 (1966); G. R. Satchler, *ibid.* **45**, 197 (1963).
[17] M. Z. Rahman Khan, Nucl. Phys. **76**, 475 (1965).
[18] J. K. Dickens and F. G. Perey, Phys. Rev. **138**, B1080 (1965); J. K. Dickens, *ibid.* **143**, 758 (1966).
[19] J. W. Luetzelschwab, Ph.D. thesis, Washington University, 1968 (unpublished).
[20] P. W. Allison, Rev. Sci. Instr. **35**, 1728 (1964).
[21] B. M. Bardin and M. E. Rickey, Rev. Sci. Instr. **35**, 902 (1964).
[22] R. Smythe, Rev. Sci. Instr. **35**, 1197 (1964).

barrier detectors. Before entering the detectors, the scattered particles passed through a circular aperture that defined the solid angle. The angular resolution at forward angles ($\theta < 52°$) was approximately 0.4°, at intermediate angles ($52° < \theta < 84°$) approximately 1°, and at back angles ($\theta > 84°$) approximately 2°. Measurements at overlapping angles for the different angular regions were recorded in order to establish the relative normalization to within $\pm 2\%$. The ΔE-E' detector assembly was mounted on one of two remotely controlled arms; the uncertainty of the angle indicating mechanism, which determines the maximum relative uncertainty between detector angles, was $\pm 0.05°$. The uncertainty of the absolute angle relative to the beam line, which was determined by measuring the elastic yield both left and right of 0°, was $\pm 0.1°$.

Pulses from particles other than ^{3}He were excluded from the pulse-height spectra with a mass identification system. After preamplification, coincident pulses from the transmission (ΔE) and stopping (E') detectors were combined with a linear adder to give a pulse proportional to the total energy, $E = E' + \Delta E$. Total-energy (E) pulses and ΔE pulses were amplified and fed to an analog multiplier[23] that produced a pulse proportional to the product $\Delta E(E + E_0 + k\Delta E)$, which is approximately proportional to the product of the mass and the square of the charge of the detected particle. E_0 and k are constants which were adjusted to give the best separation of the mass peaks corresponding to ^{3}He and α particles. Typical ratios of the height of the ^{3}He mass peak to that of the ^{3}He-α valley were 70:1. Thus, with proper coincidence and gating, virtually all pulses from particles other than ^{3}He were excluded from the pulse-height spectra recorded in a 512-channel pulse-height analyzer.

An auxiliary detector mounted on the other arm in the scattering chamber was used for monitoring the elastic intensity at fixed angles. Monitor pulses within the elastic peak were fed to the live-charge channel of the pulse-height analyzer and simultaneously to a fast scaler. The analyzer accepted these pulses only when it was not busy analyzing total-energy pulses from the ΔE-E' assembly, and the ratio of the live-charge count to the monitor-scaler count was used to make corrections for the analyzer dead time. For all angles the ratio of the monitor count to the Faraday count also served as a consistency check; deviations of this ratio were always less than 2%.

Table I lists the targets used in this experiment. With the exception of ^{27}Al, ^{115}In, and ^{116}Sn, all targets were self-supporting rolled foils.[24] The ^{27}Al target was a self-supporting commercial foil, and the ^{115}In and ^{116}Sn targets were fabricated by evaporation onto 20-μg/cm^2 carbon films.[25] The areal density of each target was determined, to within $\pm 5\%$, with an α-particle-thickness gauge.[19,26] The beam energy lost in the different targets was typically between 200 and 600 keV.

TABLE I. Targets used in this study.

Target	Areal density (mg/cm^2)	Isotopic purity (%)
^{27}Al	2.36	100 (nat.)
^{51}V	1.09	99.75 (nat.)
^{59}Co	2.97	100 (nat.)
^{60}Ni	5.30	99.79
^{89}Y	4.27	100 (nat.)
^{90}Zr	6.50	97.65
^{114}Cd	4.20	99.09
^{115}In [a]	1.59	95.84 (nat.)
^{115}In [b]	3.30	95.84 (nat.)
^{116}Sn	5.58	95.74

[a] This target was used for the 30-MeV data.
[b] This target was used for the 35-MeV data.

The energy of the first excited state of each of the nuclei studied is large enough so that the over-all resolution achieved was adequate in all cases for distinguishing between the elastic and any inelastic peaks in the pulse-height spectra.

III. EXPERIMENTAL RESULTS

Elastic yields were extracted with a computer program[27] that fit standard reference peaks to the peaks in the pulse-height spectra. Another program[27] was used to convert the cross sections derived from these yields and the corresponding angles to the barycentric system. The differential cross sections tabulated in Table II and plotted in Figs. 1–4 are for the barycentric system. A small renormalization factor determined by the procedure described in Sec. IV has been applied to these reported cross sections.

Sufficient counts were recorded at most angles so that statistical uncertainties in the elastic yields became less than 5%. However, the counting times needed to achieve a 5% statistical uncertainty for some back-angle points were greater than the available running times; consequently, some back-angle yields had statistical uncertainties as large as 20%. For a couple of the targets, and only at back angles, there was an observable overlapping of an inelastic peak with the elastic, and in these cases the uncertainty in the in-

[23] V. Radeka, IEEE Trans. Nucl. Sci. **NS-11**, 302 (1964); V. Radeka, Brookhaven National Laboratory Report No. BNL 7867 (unpublished).
[24] Rolled by F. Karasek of Microfoils, Argonne, Ill.
[25] Purchased from Yissum Research and Development Co., Jerusalem, Israel.
[26] M. A. Farouk, M. H. Nassef, A. Z. El-Behay, and I. I. Zaloubovsky, Nucl. Instr. Methods **35**, 210 (1965).
[27] D. D. Borlin, Ph.D. thesis, Washington University, 1967 (unpublished).

TABLE II. Measured elastic cross sections for 30-MeV ^{3}He scattered from ^{27}Al, ^{51}V, ^{59}Co, ^{60}Ni, ^{89}Y, ^{90}Zr, ^{114}Cd, ^{115}In, and ^{116}Sn, and 35-MeV ^{3}He scattered from ^{59}Co, ^{60}Ni, ^{115}In, and ^{116}Sn.

^{27}Al at 29.6 MeV	
$\theta_{c.m.}$ (deg)	$\sigma_{c.m.}$ (mb/sr)
6.68	6.59×10^{4}
8.90	2.29×10^{4}
11.12	9.96×10^{3}
13.35	4.39×10^{3}
15.57	1.98×10^{3}
17.78	7.08×10^{2}
20.00	2.71×10^{2}
22.21	2.13×10^{2}
24.43	2.12×10^{2}
26.63	1.83×10^{2}
28.84	1.27×10^{2}
31.04	7.29×10^{1}
33.24	2.92×10^{1}
35.43	9.19
37.62	9.63
39.81	1.41×10^{1}
41.99	1.57×10^{1}
44.16	1.34×10^{1}
46.33	9.85
48.50	5.27
50.66	2.16
52.81	8.33×10^{-1}
54.96	8.08×10^{-1}
58.17	1.39
61.37	1.43
64.55	9.30×10^{-1}
67.72	3.34×10^{-1}
70.87	1.20×10^{-1}
74.00	1.33×10^{-1}
77.12	2.42×10^{-1}
80.22	2.57×10^{-1}
83.31	1.84×10^{-1}
86.38	1.22×10^{-1}
89.43	6.52×10^{-2}
92.46	4.47×10^{-2}
95.47	3.36×10^{-2}
98.47	2.98×10^{-2}
102.40	2.57×10^{-2}
106.40	3.15×10^{-2}
111.20	3.75×10^{-2}
116.10	3.68×10^{-2}
120.90	3.49×10^{-2}
125.60	2.50×10^{-2}
130.30	2.27×10^{-2}
133.40	2.01×10^{-2}
137.10	2.04×10^{-2}
140.80	1.92×10^{-2}
144.40	2.07×10^{-2}
148.10	1.86×10^{-2}
151.70	1.41×10^{-2}
155.30	9.47×10^{-3}
158.90	8.31×10^{-3}
162.50	1.15×10^{-2}
^{51}V at 29.6 MeV	
6.57	3.26×10^{5}
8.69	9.77×10^{4}
10.81	4.07×10^{4}
12.92	1.88×10^{4}
16.10	5.55×10^{3}
19.27	1.85×10^{3}
22.44	9.83×10^{2}
25.60	5.34×10^{2}
28.77	2.25×10^{2}
31.92	1.05×10^{2}
35.08	7.52×10^{1}
38.22	6.17×10^{1}
41.37	3.38×10^{1}
44.50	1.26×10^{1}
47.63	6.94
50.75	7.18
53.87	7.04
56.98	4.71
60.08	2.46
63.17	1.16
66.26	7.80×10^{-1}
69.33	6.36×10^{-1}
72.40	5.69×10^{-1}
75.46	4.49×10^{-1}
78.51	3.60×10^{-1}
81.55	2.98×10^{-1}
84.58	1.85×10^{-1}
87.61	1.07×10^{-1}
90.62	5.49×10^{-2}
93.62	3.71×10^{-2}
96.62	4.49×10^{-2}
99.60	5.99×10^{-2}
103.60	5.23×10^{-2}
107.50	3.33×10^{-2}
111.50	1.43×10^{-2}
115.40	7.05×10^{-3}
119.30	8.98×10^{-3}
123.20	1.36×10^{-2}
127.00	1.31×10^{-2}
130.90	1.28×10^{-2}
134.70	7.03×10^{-3}
138.60	2.92×10^{-3}
142.40	1.82×10^{-3}
146.20	2.84×10^{-3}
150.00	4.73×10^{-3}
153.80	5.11×10^{-3}
157.60	4.66×10^{-3}
^{59}Co at 29.5 MeV	
6.52	4.26×10^{5}
8.62	1.51×10^{5}
10.72	5.97×10^{4}
12.83	2.77×10^{4}
15.98	9.24×10^{3}
19.12	3.24×10^{3}
22.27	1.61×10^{3}
25.41	8.45×10^{2}
28.55	3.70×10^{2}
31.69	1.73×10^{2}
34.82	1.18×10^{2}
37.95	8.19×10^{1}
41.07	4.42×10^{1}
44.19	2.21×10^{1}
47.30	1.50×10^{1}
50.41	1.25×10^{1}
53.51	8.91
56.60	5.20
59.69	2.77
62.77	1.91
65.84	1.62
68.91	1.28
71.97	8.72×10^{-1}
75.02	5.81×10^{-1}
78.06	3.70×10^{-1}
81.10	2.90×10^{-1}
84.12	2.17×10^{-1}
87.14	1.64×10^{-1}
90.16	1.22×10^{-1}
93.16	9.79×10^{-2}
96.15	8.44×10^{-2}
99.14	6.92×10^{-2}
103.10	4.14×10^{-2}
107.10	2.31×10^{-2}
111.00	1.97×10^{-2}
114.90	1.95×10^{-2}

TABLE II. (*Continued*).

$\theta_{c.m.}$ (deg)	$\sigma_{c.m.}$ (mb/sr)
118.90	1.62×10^{-2}
122.80	1.24×10^{-2}
126.60	7.43×10^{-3}
130.50	5.26×10^{-3}
134.40	4.59×10^{-3}
138.20	4.88×10^{-3}
142.10	4.13×10^{-3}
145.90	3.33×10^{-3}
149.80	2.79×10^{-3}
153.60	2.69×10^{-3}
157.40	2.59×10^{-3}
161.20	2.36×10^{-3}
165.00	2.50×10^{-3}
^{60}Ni at 29.5 MeV	
28.60	4.53×10^{2}
31.74	2.18×10^{2}
34.87	1.45×10^{2}
37.99	9.72×10^{1}
41.11	5.34×10^{1}
44.23	2.80×10^{1}
47.34	1.85×10^{1}
50.44	1.50×10^{1}
53.54	1.14×10^{1}
56.63	6.61
59.72	3.23
62.80	2.24
65.87	2.02
68.93	1.55
71.99	1.03
75.04	6.80×10^{-1}
78.08	4.51×10^{-1}
81.12	3.36×10^{-1}
84.15	2.66×10^{-1}
87.17	2.06×10^{-1}
90.18	1.46×10^{-1}
93.18	1.16×10^{-1}
96.17	9.51×10^{-2}
99.16	7.42×10^{-2}
103.20	4.57×10^{-2}
107.10	2.82×10^{-2}
111.10	1.88×10^{-2}
115.00	2.13×10^{-2}
118.90	2.01×10^{-2}
122.80	1.45×10^{-2}
126.70	1.01×10^{-2}
130.60	6.83×10^{-3}
134.50	7.51×10^{-3}
138.30	7.25×10^{-3}
142.20	7.62×10^{-3}
146.00	6.73×10^{-3}
149.80	5.69×10^{-3}
153.70	5.33×10^{-3}
157.50	4.96×10^{-3}
161.30	5.62×10^{-3}
165.10	6.33×10^{-3}
^{89}Y at 29.6 MeV	
6.31	1.11×10^{6}
8.38	3.31×10^{5}
10.44	1.44×10^{5}
12.51	7.26×10^{4}
15.61	2.87×10^{4}
18.71	1.31×10^{4}
21.81	5.85×10^{3}
24.90	2.94×10^{3}
27.99	1.47×10^{3}
31.08	7.56×10^{2}
34.17	4.66×10^{2}
37.26	2.88×10^{2}
40.34	1.57×10^{2}
43.42	9.05×10^{1}
46.49	5.90×10^{1}
49.56	4.25×10^{1}
52.63	3.07×10^{1}
55.69	1.97×10^{1}
58.75	1.21×10^{1}
61.80	8.13
64.85	5.65
67.89	4.19
70.93	3.14
73.97	2.47
77.00	1.70
80.02	1.19
83.04	7.92×10^{-1}
86.05	5.46×10^{-1}
89.06	4.68×10^{-1}
92.06	3.88×10^{-1}
95.06	3.19×10^{-1}
98.05	2.30×10^{-1}
102.00	1.39×10^{-1}
106.00	8.54×10^{-2}
110.00	7.11×10^{-2}
113.90	6.93×10^{-2}
117.90	5.58×10^{-2}
121.80	3.55×10^{-2}
125.70	2.07×10^{-2}
129.60	1.50×10^{-2}
133.60	1.74×10^{-2}
137.50	1.81×10^{-2}
141.50	1.59×10^{-2}
145.30	9.85×10^{-3}
149.20	5.63×10^{-3}
153.10	6.15×10^{-3}
157.00	7.72×10^{-3}
160.90	8.74×10^{-3}
164.70	7.82×10^{-3}
^{90}Zr at 29.8 MeV	
15.71	3.11×10^{4}
18.81	1.36×10^{4}
21.90	6.18×10^{3}
25.00	3.17×10^{3}
28.09	1.62×10^{3}
31.18	8.31×10^{2}
34.26	5.05×10^{2}
37.35	3.05×10^{2}
40.43	1.69×10^{2}
43.50	9.63×10^{1}
46.58	6.39×10^{1}
49.65	4.48×10^{1}
52.71	3.24×10^{1}
55.77	2.13×10^{1}
58.83	1.35×10^{1}
61.88	8.69
64.93	6.08
67.98	4.55
71.01	3.35
74.05	2.63
77.08	1.89
80.10	1.28
83.12	8.92×10^{-1}
86.13	6.50×10^{-1}
89.14	5.20×10^{-1}
92.14	4.54×10^{-1}
95.14	3.42×10^{-1}
98.13	2.63×10^{-1}
102.10	1.60×10^{-1}
106.10	1.08×10^{-1}
110.00	8.57×10^{-2}
114.00	7.99×10^{-2}

TABLE II. (*Continued*).

$\theta_{c.m.}$ (deg)	$\sigma_{c.m.}$ (mb/sr)
117.90	6.72×10^{-2}
121.90	4.81×10^{-2}
125.80	2.97×10^{-2}
129.70	1.77×10^{-2}
133.60	1.97×10^{-2}
137.50	1.93×10^{-2}
141.40	1.65×10^{-2}
145.30	1.06×10^{-2}
149.20	7.20×10^{-3}
153.10	6.42×10^{-3}
157.00	7.57×10^{-3}
160.90	9.82×10^{-3}
164.70	9.03×10^{-3}
^{114}Cd at 29.7 MeV	
6.47	1.20×10^{6}
8.52	4.30×10^{5}
10.57	1.89×10^{5}
12.63	9.52×10^{4}
15.70	4.46×10^{4}
18.78	2.28×10^{4}
21.86	1.19×10^{4}
24.93	6.26×10^{3}
28.00	3.40×10^{3}
31.07	1.83×10^{3}
34.14	1.08×10^{3}
37.21	6.63×10^{2}
40.27	3.87×10^{2}
43.33	2.35×10^{2}
46.39	1.56×10^{2}
49.44	9.72×10^{1}
52.50	6.24×10^{1}
55.54	4.27×10^{1}
58.59	2.95×10^{1}
61.63	2.03×10^{1}
64.67	1.31×10^{1}
67.70	8.91
70.73	6.15
73.76	4.43
76.78	3.32
79.80	2.14
82.81	1.74
85.82	1.18
88.83	8.57×10^{-1}
91.83	6.48×10^{-1}
94.83	4.96×10^{-1}
97.82	3.76×10^{-1}
101.80	2.62×10^{-1}
105.80	1.93×10^{-1}
109.80	1.39×10^{-1}
113.70	1.08×10^{-1}
117.70	7.44×10^{-2}
121.60	5.72×10^{-2}
125.60	4.28×10^{-2}
129.50	3.54×10^{-2}
133.40	2.49×10^{-2}
137.40	2.07×10^{-2}
141.30	1.96×10^{-2}
145.20	1.67×10^{-2}
149.10	1.56×10^{-2}
153.00	1.25×10^{-2}
156.90	1.15×10^{-2}
160.80	8.83×10^{-3}
164.70	9.20×10^{-3}
^{115}In at 29.8 MeV	
6.47	1.45×10^{6}
8.52	4.79×10^{5}
10.57	2.08×10^{5}
15.75	4.64×10^{4}
18.83	2.29×10^{4}
21.85	1.19×10^{4}
24.93	6.86×10^{3}
28.00	3.47×10^{3}
31.07	1.91×10^{3}
34.13	1.18×10^{3}
37.20	6.97×10^{2}
40.31	3.93×10^{2}
43.37	2.56×10^{2}
46.43	1.52×10^{2}
49.48	9.95×10^{1}
52.54	6.51×10^{1}
55.58	4.28×10^{1}
58.63	3.03×10^{1}
61.67	2.15×10^{1}
64.71	1.51×10^{1}
67.74	1.05×10^{1}
70.77	7.33
73.80	5.35
76.82	3.86
79.84	2.92
82.85	2.14
85.78	1.52
88.79	1.06
91.79	8.43×10^{-1}
94.78	6.67×10^{-1}
97.78	5.22×10^{-1}
101.80	3.63×10^{-1}
105.80	2.53×10^{-1}
109.70	1.81×10^{-1}
113.70	1.34×10^{-1}
117.70	1.07×10^{-1}
121.60	8.64×10^{-2}
125.60	6.37×10^{-2}
129.50	5.72×10^{-2}
133.40	4.41×10^{-2}
137.30	3.52×10^{-2}
141.30	3.59×10^{-2}
146.20	2.60×10^{-2}
151.10	2.40×10^{-2}
155.90	1.98×10^{-2}
160.80	1.59×10^{-2}
^{116}Sn at 29.5 MeV	
6.57	1.30×10^{6}
8.62	4.52×10^{5}
10.67	1.94×10^{5}
12.72	1.03×10^{5}
14.77	5.91×10^{4}
16.83	3.77×10^{4}
18.88	2.49×10^{4}
20.92	1.60×10^{4}
22.97	1.08×10^{4}
25.02	7.36×10^{3}
27.07	4.95×10^{3}
33.21	1.59×10^{3}
35.25	1.10×10^{3}
37.29	7.59×10^{2}
39.34	5.51×10^{2}
41.38	4.03×10^{2}
43.42	2.98×10^{2}
45.45	2.18×10^{2}
47.49	1.62×10^{2}
49.53	1.23×10^{2}
51.56	9.09×10^{1}
53.59	7.00×10^{1}
55.62	5.40×10^{1}
57.65	4.30×10^{1}
59.68	3.36×10^{1}
61.71	2.68×10^{1}
64.75	1.95×10^{1}

TABLE II. (*Continued*).

$\theta_{c.m.}$ (deg)	$\sigma_{c.m.}$ (mb/sr)
67.78	1.37×10^{1}
70.81	9.48
73.83	6.72
76.86	5.18
79.87	4.05
82.89	3.01
85.90	2.19
88.90	1.59
91.90	1.23
94.90	8.91×10^{-1}
97.90	7.55×10^{-1}
101.90	5.60×10^{-1}
105.90	4.42×10^{-1}
109.80	3.10×10^{-1}
113.80	2.32×10^{-1}
117.70	1.90×10^{-1}
121.70	1.45×10^{-1}
125.60	1.14×10^{-1}
129.50	8.92×10^{-2}
133.40	6.86×10^{-2}
137.30	5.87×10^{-2}
141.30	4.72×10^{-2}
145.20	3.90×10^{-2}
149.10	3.56×10^{-2}
153.00	2.96×10^{-2}
156.90	2.93×10^{-2}
160.80	1.93×10^{-2}
164.70	2.42×10^{-2}
^{59}Co at 34.8 MeV	
6.63	3.35×10^{5}
8.73	9.41×10^{4}
10.83	3.87×10^{4}
12.93	1.71×10^{4}
16.08	4.66×10^{3}
19.23	1.87×10^{3}
22.38	9.72×10^{2}
25.52	4.00×10^{2}
28.66	1.60×10^{2}
31.80	1.14×10^{2}
34.93	7.40×10^{1}
38.06	3.60×10^{1}
41.18	1.41×10^{1}
44.30	1.09×10^{1}
47.41	9.54
50.51	5.63
53.61	2.48
56.71	1.54
59.80	1.25
62.88	9.08×10^{-1}
65.95	5.36×10^{-1}
69.02	3.55×10^{-1}
72.07	2.98×10^{-1}
75.12	2.51×10^{-1}
78.17	1.33×10^{-1}
81.20	6.38×10^{-2}
84.23	4.80×10^{-2}
87.25	5.89×10^{-2}
90.26	5.98×10^{-2}
93.26	4.35×10^{-2}
96.26	2.11×10^{-2}
99.25	1.01×10^{-2}
103.20	8.44×10^{-3}
107.20	1.02×10^{-2}
111.10	7.50×10^{-3}
115.00	5.20×10^{-3}
119.00	3.33×10^{-3}
122.90	2.47×10^{-3}
127.70	2.18×10^{-3}
132.60	2.26×10^{-3}
137.40	1.95×10^{-3}
142.20	1.18×10^{-3}

$\theta_{c.m.}$ (deg)	$\sigma_{c.m.}$ (mb/sr)
^{60}Ni at 35.1 MeV	
6.62	3.32×10^{5}
8.72	1.01×10^{5}
10.82	4.86×10^{4}
12.92	1.79×10^{4}
16.07	5.10×10^{3}
19.22	1.99×10^{3}
22.36	1.03×10^{3}
25.50	4.99×10^{2}
28.64	2.03×10^{2}
31.77	1.36×10^{2}
34.90	9.34×10^{1}
38.03	4.27×10^{1}
41.15	1.81×10^{1}
44.26	1.46×10^{1}
47.37	1.32×10^{1}
50.48	7.64
53.58	3.45
56.67	1.96
59.75	1.68
62.83	1.19
65.91	7.54×10^{-1}
68.97	4.43×10^{-1}
72.03	3.93×10^{-1}
75.08	3.26×10^{-1}
78.02	1.75×10^{-1}
81.05	7.73×10^{-2}
84.08	5.68×10^{-2}
87.10	7.06×10^{-2}
90.11	7.50×10^{-2}
93.11	5.46×10^{-2}
96.11	2.47×10^{-2}
99.10	6.55×10^{-3}
103.10	7.40×10^{-3}
107.00	1.30×10^{-2}
111.00	1.14×10^{-2}
114.90	6.22×10^{-3}
118.80	1.82×10^{-3}
122.70	1.48×10^{-3}
126.60	2.01×10^{-3}
130.50	3.63×10^{-3}
134.40	2.76×10^{-3}
138.20	1.98×10^{-3}
142.10	1.16×10^{-3}
151.60	1.06×10^{-3}
^{115}In at 35.3 MeV	
6.33	1.10×10^{6}
8.39	3.53×10^{5}
10.44	1.47×10^{5}
12.49	7.69×10^{4}
15.57	3.36×10^{4}
18.64	1.44×10^{4}
21.72	6.98×10^{3}
24.79	3.24×10^{3}
27.86	1.64×10^{3}
30.93	8.84×10^{2}
34.00	4.87×10^{2}
37.07	2.50×10^{2}
40.13	1.45×10^{2}
43.19	9.74×10^{1}
46.25	5.93×10^{1}
49.30	3.52×10^{1}
52.36	2.26×10^{1}
55.40	1.51×10^{1}
58.45	1.02×10^{1}
61.49	6.37
64.53	4.46
67.56	2.99
70.59	2.01
73.62	1.37

TABLE II. (*Continued*).

$\theta_{c.m.}$ (deg)	$\sigma_{c.m.}$ (mb/sr)
76.64	1.03
79.66	7.72×10^{-1}
82.67	5.06×10^{-1}
85.68	3.13×10^{-1}
88.69	2.53×10^{-1}
91.69	1.91×10^{-1}
94.69	1.58×10^{-1}
97.68	1.17×10^{-1}
101.70	6.93×10^{-2}
105.70	4.40×10^{-2}
109.60	3.56×10^{-2}
113.60	2.74×10^{-2}
117.60	1.67×10^{-2}
121.50	1.25×10^{-2}
126.40	9.29×10^{-3}
131.40	6.32×10^{-3}
136.30	4.60×10^{-3}
^{116}Sn at 35.2 MeV	
18.64	1.57×10^{4}
21.71	7.42×10^{3}
24.79	3.62×10^{3}
27.86	1.81×10^{3}
30.93	9.81×10^{2}
34.00	5.33×10^{2}
37.06	2.89×10^{2}
40.12	1.75×10^{2}
43.18	1.13×10^{2}
46.24	6.82×10^{1}
49.29	4.05×10^{1}
52.35	2.56×10^{1}
55.39	1.81×10^{1}
58.44	1.18×10^{1}
61.48	7.71
64.52	5.23
67.55	3.52
70.58	2.35
73.61	1.71
76.63	1.28
79.65	9.61×10^{-1}
82.66	6.49×10^{-1}
85.67	4.17×10^{-1}
88.68	2.86×10^{-1}
91.68	2.32×10^{-1}
94.67	1.78×10^{-1}
97.67	1.50×10^{-1}
101.70	8.18×10^{-2}
105.70	5.36×10^{-2}
109.60	4.25×10^{-2}
113.60	3.35×10^{-2}
117.60	2.34×10^{-2}
121.50	1.25×10^{-2}
126.40	1.01×10^{-2}
131.40	4.85×10^{-3}
136.30	6.10×10^{-3}
141.20	4.14×10^{-3}

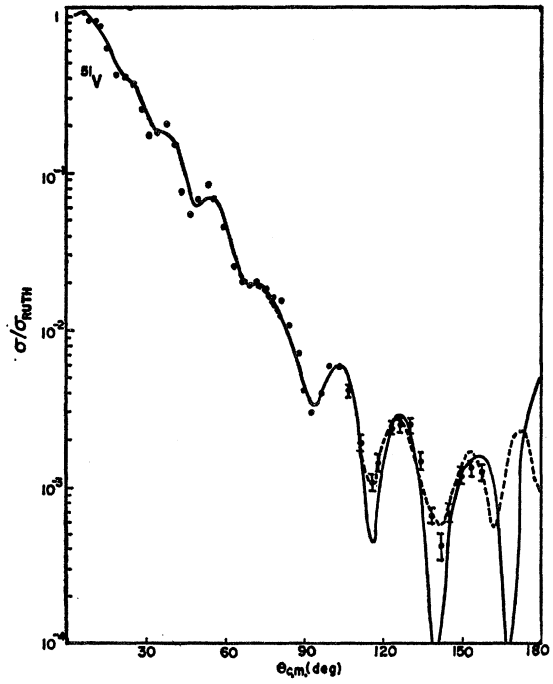

FIG. 1. Optical-model fits to the 30-MeV data for ^{51}V. The solid curve (——) is the best fit obtained without the spin-orbit potential, and the dashed curve (– – –) is the fit obtained with the spin-orbit potential. The potential parameters that produce these fits are given in Table IV, families d and $d-1$.

elastic subtraction contributed additionally to the relative uncertainty in the elastic yield. In some rare cases this subtraction uncertainty contributed as much as 20%. The resulting relative uncertainties for all the data are indicated in Figs. 1–4 by appropriate error bars wherever they are greater than the size of the points.

IV. OPTICAL-MODEL RESULTS

The optical-model calculations were performed with a slightly modified form of the computer code of Perey.[28] The optical potential $V(r)$ is defined to be

$$V(r) = -Vf(r; a, r_0) - iWf(r; a', r_0') + V_C, \quad (1)$$

where V and W are the real and imaginary well depths, $f(r; a, r_0)$ is the Woods-Saxon form factor,

$$f(r; a, r_0) = \left(1+\exp\frac{r-r_0A^{1/3}}{a}\right)^{-1},$$

and A is the atomic number of the target nucleus. V_C is the Coulomb potential of the charge of the target nucleus uniformly distributed throughout the volume of a sphere of radius $r_{0C}A^{1/3}$. Unless otherwise specified, all calculations were performed with $r_{0C}=1.25$ F. No

[28] F. G. Perey, Phys. Rev. **131**, 745 (1963).

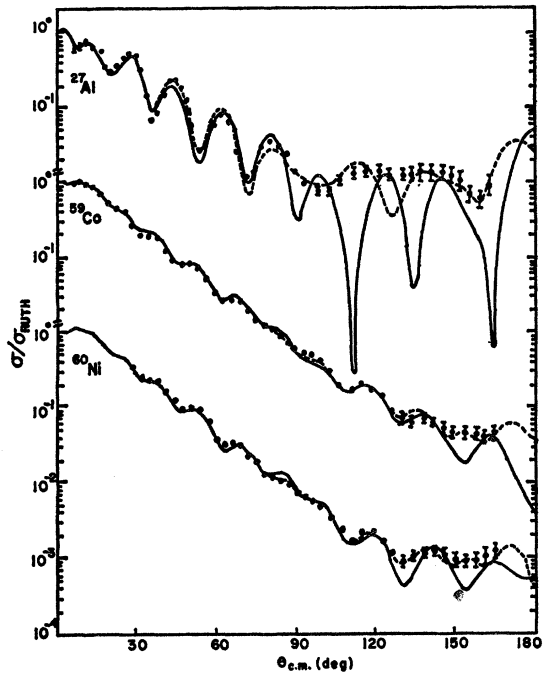

FIG. 2. Optical-model fits to the 30-MeV data for ^{27}Al, ^{59}Co, and ^{60}Ni. The solid curves (——) are the best fits obtained without the spin-orbit potential, and the dashed curves (– – –) are the fits obtained with the spin-orbit potential. The potential parameters that produce these fits are listed in Table IV, families d and $d-1$, and Table V, families c and $c-1$.

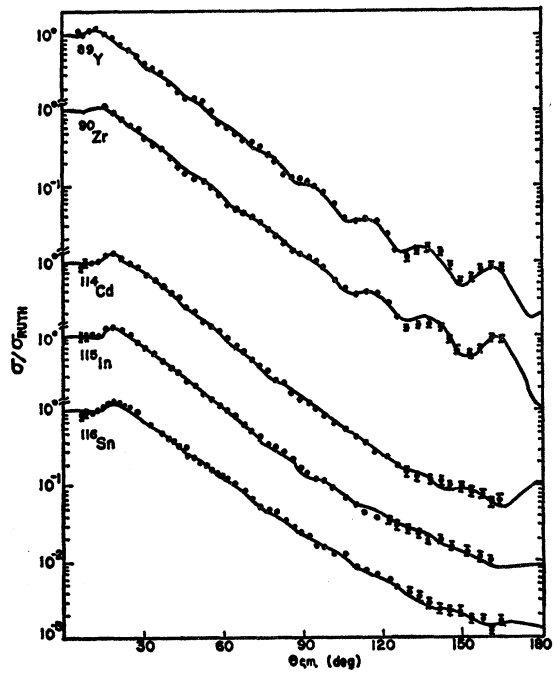

FIG. 3. Optical-model fits to the 30-MeV data for ^{89}Y, ^{90}Zr, ^{114}Cd, ^{115}In, and ^{116}Sn. In these cases no attempt to include the spin-orbit potential was made; the above fits are quite satisfactory without the spin-orbit potential. The parameters that produce these fits are listed in Table IV, families d.

calculations were performed with the inclusion of a surface-peaked imaginary potential. If a spin-orbit potential was included, the Thomas form was added to the above potential:

$$V(r)_{so}=+V_{so}\left(\frac{\hbar}{m_\pi c}\right)^2\frac{\boldsymbol{\sigma}\cdot\mathbf{l}}{r}\frac{d}{dr}f(r;a,r_0), \qquad (2)$$

where $\boldsymbol{\sigma}$ is the Pauli spin matrix[29] and m_π is the pion mass. No calculations were performed with the inclusion of an imaginary spin-orbit term.

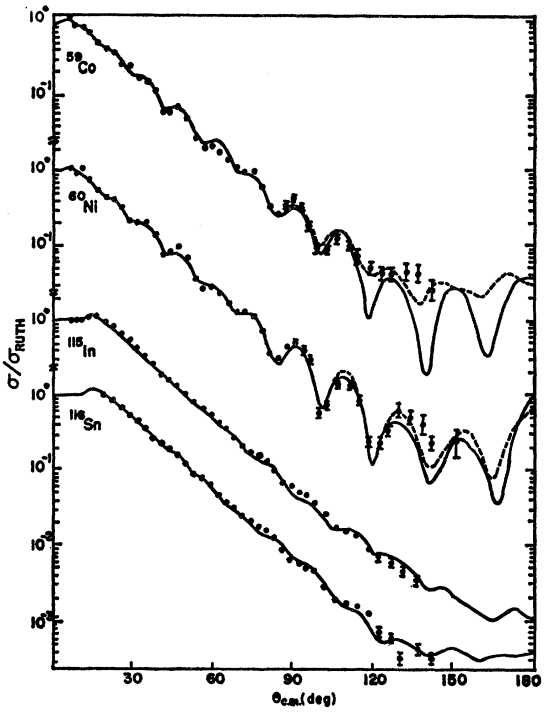

FIG. 4. Optical-model fits to the 35-MeV data for ^{59}Co, ^{60}Ni, ^{115}In, and ^{116}Sn. The solid curves (——) are the best fits obtained without the spin-orbit potential, and the dashed curves (– – –) are the fits obtained with the spin-orbit potential. No attempt was made to include the spin-orbit potential for ^{115}In and ^{116}Sn. The parameters that produce these fits are listed in Table IV, families d and $d-1$.

The code varied selected parameters until a minimum value of χ^2 was obtained, with

$$\chi^2\equiv N^{-1}\sum_{i=1}^{N}\left[\frac{\sigma_{\text{theoret}}(\theta_i)-R\sigma_{\text{expt}}(\theta_i)}{\Delta\sigma_{\text{expt}}(\theta_i)}\right]^2, \qquad (3)$$

where σ_{theoret} and σ_{expt}, respectively, are the calculated and measured differential cross sections, $\Delta\sigma_{\text{expt}}$ is the assigned relative uncertainty, N is the number of cross

[29] Several different factors in the spin-orbit potential have been used in the literature, and the resulting well depths often differ by about a factor of 2. See, for example, Refs. 1, 8, and 13.

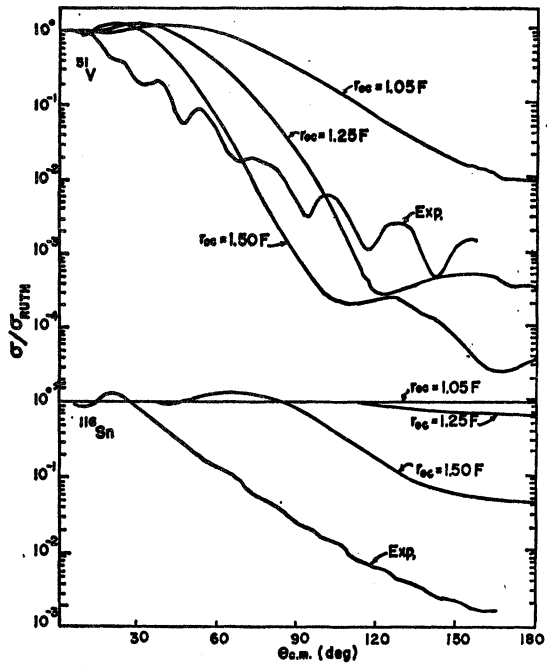

FIG. 5. Calculated Coulomb cross sections for 30-MeV ^{3}He projectiles scattered from the charge of ^{51}V and ^{116}Sn. These Coulomb (extended charge) cross sections were calculated by setting all the nuclear wells to zero in the optical-potential code. The Coulomb cross sections are plotted relative to the Rutherford (point-charge) cross sections. The Coulomb cross sections for several different values of the charge radius parameter r_{0C} are shown. The curve labeled Exp represents a smooth curve drawn through the measured cross sections.

sections included in the fit, and R is a renormalization factor.[30]

Previous optical-model studies of charged-particle scattering have shown that the nuclear potential parameters are quite insensitive to the particular choice of the radius parameter for the Coulomb part of the potential, r_{0C}, provided only that it is taken somewhere between 1.0 and 1.5 F. Our results agreed: Equally good fits with variations of less than 1% in the nuclear parameters were obtained for different choices of r_{0C} within this range. This insensitivity of the combined Coulomb and nuclear scattering to r_{0C} does not mean, however, that the pure Coulomb part σ_{Coul} is insensitive to r_{0C}. On the contrary, Fig. 5 shows a strong dependence of σ_{Coul} on the choice of the radius of the charge distribution. As has been customary in the graphical presentation of differential cross sections for charged projectiles, the Coulomb cross sections in Fig. 5 are plotted relative to the Rutherford (point-charge) cross section. The curves of Fig. 5, which were calculated with the Perey code by setting the depths of all the nuclear wells to zero, show that σ_{Coul} for ^{51}V is quite sensitive to the choice of r_{0C} and that, for r_{0C} between 1.25 and 1.50 F, the gross structure of the angular distribution is nearly reproduced by σ_{Coul} alone. The practice of comparing measured cross sections with σ_{Ruth} overemphasises the "Rutherford anomaly," which to a certain extent can be accounted for by merely considering the effect of an extended charge distribution. Since it is the nuclear interaction that is of primary interest, and since it is presumably the nuclear potential that causes deviations from the relatively well-understood Coulomb potential, it seems that angular distributions plotted relative to σ_{Coul} instead of relative to σ_{Ruth} would display more information about the specifically nuclear part of the cross sections. An example of a plot of $\sigma/\sigma_{\text{Coul}}$ for ^{51}V is shown in Fig. 6, which should be compared with the more conventional presentation shown in Fig. 1. Convention will prevail, however, throughout the rest of this paper.

For charged projectiles, elastic scattering at small angles is dominated by the Coulomb part of the optical potential, and in this region of small angles Coulomb scattering is equivalent to Rutherford scattering. Therefore, ratios of the measured cross section to the Rutherford cross section, $\sigma/\sigma_{\text{Ruth}}$, should approach unity as the angles approach zero. However, because σ_{Ruth} is inversely proportional to $E^2 \sin^4\frac{1}{2}\theta$, where E is the projectile energy and θ is the barycentric scattering angle, and because the measured yield is proportional to the areal density of target nuclei, any systematic errors in the measurements of E, θ, or the target thickness cause the small-angle ratios of $\sigma/\sigma_{\text{Ruth}}$ to deviate from unity. Consequently, if these small-angle ratios did not initially agree with those predicted by the optical calculation, R was changed to produce optimum small-angle agreement. In this way the absolute uncertainty in the differential cross sections was reduced to within $\pm 4\%$, independently of systematic errors in the initial calculations of the measured cross sections.

Since calculated small-angle cross sections are highly insensitive to the particular choice of nuclear param-

[30] A new goodness-of-fit criterion that enhances the sensitivity in the back-angle region and reduces the sensitivity in the forward-angle region has been suggested in a recent paper by Robinson *et al.* [C. P. Robinson, J. P. Aldridge, J. John, and R. H. Davis, Phys. Rev. **171**, 1241 (1968)]. Their approach is to give less weight to $\Delta\sigma_{\text{expt}}(\theta_i)$ according to the strength of the Rutherford (point charge) cross section at θ_i:

$$g^2 \equiv B^{-1} \sum_{i=1}^{N} \left[\frac{\sigma_{\text{theoret}}(\theta_i) - R\sigma_{\text{expt}}(\theta_i)}{\Delta\sigma_{\text{expt}}(\theta_i)\sigma_{\text{Ruth}}(\theta_i)} \right]^2,$$

where the symbolism has been changed to conform with our notation and

$$B \equiv \sum_{i=1}^{N} [\sigma_{\text{Ruth}}(\theta_i)]^{-2}.$$

The definition of g^2 here includes a slightly different normalization that produces values close to 1 when the fit is visually good. We found that in all cases potential parameters obtained using g^2 were essentially the same as those obtained using the ordinary χ^2 criterion, and that the g^2 criterion did not suppress any of the basic ambiguities in the parameters. However, this new criterion was especially sensitive to the spin-orbit potential depth V_{so}, though the final values obtained for V_{so} were virtually the same as those obtained using χ^2. All the results reported here are based on the χ^2 criterion.

eters, R was determined by using parameters believed to be approximately correct. An initial search with these starting parameters and with R set to unity was performed, and R was then determined to be the multiplication factor that produced the best fit in the forward-angle region. Values of R for the different targets ranged between 0.93 and 1.12, values all within a range consistent with the systematic uncertainties involved. Searches for best-fit nuclear parameters were then performed after the appropriate renormalization was applied to the data. We found, however, that best-fit parameters obtained by allowing variation of all the nuclear parameters were quite nonunique because of the ambiguities mentioned previously. It was our desire, therefore, to suppress some of these ambiguities.

One way to suppress the continuous ambiguity between the depth and radius parameters, $V(r_0)^n$, is to choose a reasonable value for r_0 and hold it fixed in the fitting procedure. Thus, in order to investigate the nature of this ambiguity, best-fit parameter searches were performed with different fixed values for r_0 and with variation of the parameters V, a, W, r_0', a', and V_{so}. Parameter searches were performed in this way for two angular distributions: ^{51}V at 30 MeV and ^{59}Co at 35 MeV. On the basis of theoretical considerations mentioned previously, families of parameters with a real depth parameter V of about 150 MeV are preferred, and therefore a starting value of $V=150$ MeV

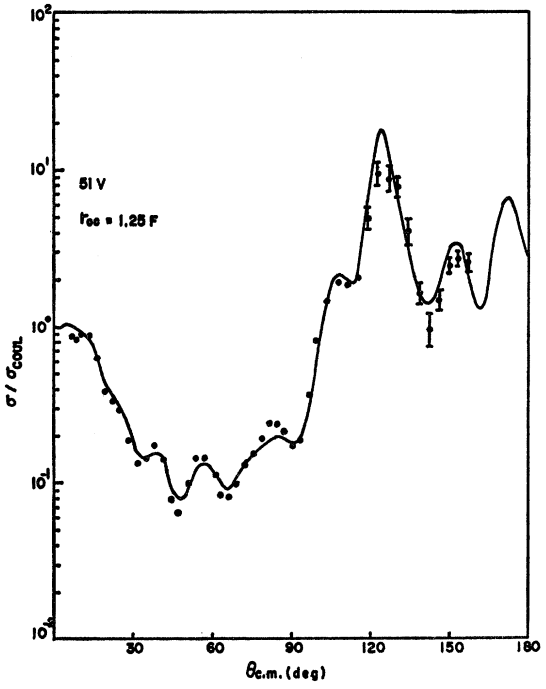

FIG. 6. Angular distribution of Fig. 1 plotted here relative to the Coulomb (extended charge) cross section. In Fig. 1 the angular distribution is plotted relative to the Rutherford (point-charge) cross section. For the above curve the charge radius parameter $r_{0C}=1.25$ F.

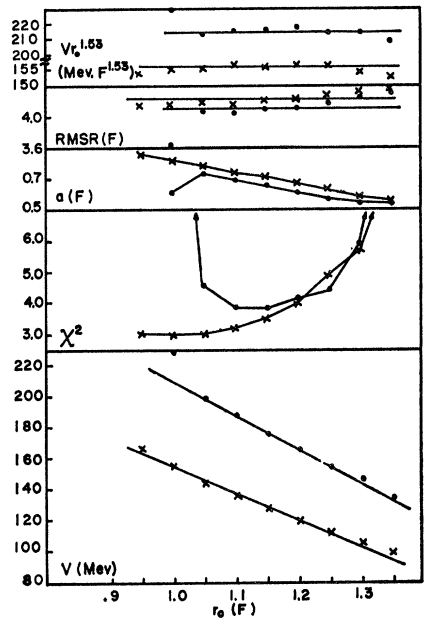

FIG. 7. Variation of the best-fit values of V and a and the corresponding values of χ^2 for different fixed values of r_0. These results are for the 30-MeV data for ^{51}V. The dependence on r_0 of the root-mean-square radius (RMSR) and of the product $V(r_0)^{1.53}$ is also shown. The crosses ($\times$) are values for the 100-MeV family of parameters and the dots ($\cdot$) are values for the 150-MeV family of parameters.

was chosen. In addition, for the sake of comparison, the "100-MeV family" for ^{51}V was also included in this investigation. The results are shown in Figs. 7 and 8. These figures show that the χ^2 minima have a broad region of comparable values for r_0 from 1.05–1.25 F and that, for the 150-MeV family for ^{51}V, they have rapidly rising values outside this region. However, no such rapid rise is observed for the lower values of r_0 for ^{59}Co and for the 100-MeV family for ^{51}V. Furthermore, results similar to these were obtained from a previous analysis of this type[3] for 43.7-MeV ^{3}He projectiles scattered from ^{58}Ni. It is apparent from these investigations that the χ^2 criterion alone limits values for the real radius parameter to lie only within a broad range from 1.05–1.25 F; to this extent the real radius is undefined by the analysis.

This ambiguity is related to the insensitivity of the elastic angular distribution to the precise shape of the scattering potential. If not the exact shape, then there must be some other properties of the scattering potential that are precisely defined. One such property seems to be the first moment for the potential or the root-mean-square radius (this property can be regarded as the expectation value for the radius, or the average radius). Thus, following a suggestion of Greenlees *et al.*,[31] root-mean-square radii (RMSR) were calcu-

[31] G. W. Greenlees, G. J. Pyle, and Y. C. Tang, Phys. Rev. Letters **17**, 33 (1966); Phys. Rev. **171**, 1115 (1968).

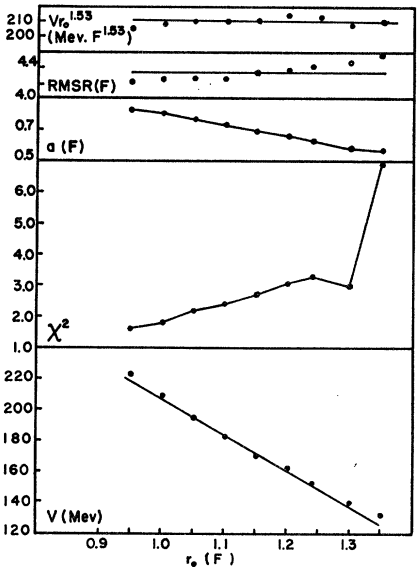

FIG. 8. Variation of the best-fit values of V and a and the corresponding values of χ^2 for different fixed values of r_0. These results are for the 35-MeV data for ^{59}Co. The dependence on r_0 of the root-mean-square radius (RMSR) and of the product $V(r_0)^{1.53}$ is also shown.

lated[32,33] with the parameters of the above analysis, and they are plotted versus r_0 at the top of Figs. 7 and 8. It can be seen that the RMSR is practically independent of the particular choice of r_0 (for r_0 between 1.05 and 1.25 F, the RMSR changes by less than 3% for ^{51}V and by less than 5% for ^{59}Co). This near-constancy of RMSR agrees with the conclusion of Greenlees *et al.*[31] that an optical-model analysis defines only the mean-square radius rather than the exact shape of the real potential. Thus, though the resulting values for r_0 and a are interdependent and ambiguous, the resulting value for the RMSR is apparently unambiguous.[34] It is interesting to note that the RMSR is constant, independently of the constancy of the product $V(r_0)^n$, with $n=1.53$ in Figs. 7 and 8.

[32] The mean-square radius of a Woods-Saxon well is a function of the radius $\mathcal{R}=r_0A^{1/3}$ and the diffuseness a (Ref. 33, Appendix C):

$$(\mathrm{RMSR})^2=\tfrac{3}{5}\mathcal{R}^2\left(1+\frac{10\pi^2a^2}{3\mathcal{R}^2}+\frac{7\pi^4a^4}{3\mathcal{R}^4}\right)\left(1+\frac{\pi^2a^2}{\mathcal{R}^2}\right)^{-1}.$$

A form of this equation appears with a misprint in the main text of Elton (Ref. 33) and in Appendix B of Hodgson (Ref. 1).

[33] L. R. B. Elton, *Nuclear Sizes* (Oxford University Press, London, 1961).

[34] This insensitivity of an optical-model analysis to the precise shape of the optical potential seems analogous to the insensitivity of low-energy neutron-proton scattering to the precise shape of the two-nucleon potential. In this case only the two parameters of the shape-independent approximation, the effective range and the scattering length, are required to produce good agreement with the data. See, for example, J. D. Jackson and J. M. Blatt, Rev. Mod. Phys. **22**, 77 (1950), or a recent nuclear physics text, such as M. A. Preston, *Physics of the Nucleus* (Addison-Wesley Publishing Co., Inc., Reading, Mass., 1962).

Because the mean-square radius [MSR=(RMSR)^2] is relatively free from ambiguity, it should have more physical meaning than $\mathcal{R}^2=r_0^2A^{2/3}$. In order to test this idea, the real potential parameters discussed below (Tables IV and V) were used to determine MSR for each target studied. The resulting values are listed in the column labeled $\mathrm{MSR_{He}}$ of Table III. (These calculations were done with parameters for the 150-MeV families.) Indeed, there may be significant physical meaning in a comparison of these values of $\mathrm{MSR_{He}}$ with corresponding values for electron scattering (MSR_e). The column labeled MSR_e in Table III lists electron scattering MSR taken from the literature.[33] The difference between $\mathrm{MSR_{He}}$ and MSR_e probably represents the extension of the nuclear potential for ^{3}He scattering beyond the potential for electron scattering, and this difference may be related to the finite range of the nuclear interaction and a possible extension of the neutron distribution beyond the proton distribution. These differences are listed in the column labeled ΔMSR in Table III and are plotted versus $A^{2/3}$ in Fig. 9. The plot shows an approximate linear dependence on $A^{2/3}$. Since there is no reason to expect the range of the two-nucleon interaction to be dependent on A, this linear increase with A suggests that the neutron distribution increasingly extends beyond the

TABLE III. Mean-square radii for ^{3}He elastic scattering and for electron scattering. The column labeled $\mathrm{MSR_{He}}$ lists the mean-square radii calculated using the real radius and diffuseness parameters of the 150-MeV families listed in Tables IV and V. For the cases of ^{27}Al, ^{51}V, ^{59}Co, and ^{60}Ni, the parameters were taken from families with the spin-orbit potential included. Where the same nucleus is listed twice, the second entry corresponds to the 35-MeV ^{3}He energy. The column labeled MSR_e lists the corresponding mean-square electron scattering radii taken from the literature.[a] The last column labeled ΔMSR lists the differences between $\mathrm{MSR_{He}}$ and MSR_e.

Nucleus	$\mathrm{MSR_{He}}$ (F^2)	MSR_e (F^2)	ΔMSR (F^2)
^{27}Al	14.5	9.2	5.3
^{51}V	17.3	12.9	4.4
^{59}Co	19.8	14.7	5.1
^{59}Co	19.1	14.7	4.4
^{60}Ni	20.2	14.8	5.4
^{60}Ni	19.5	14.8	4.7
^{89}Y	24.2	18.0	6.2
^{90}Zr	23.4	18.1	5.3
^{114}Cd	27.5	20.5	7.0
^{115}In	28.3	20.6	7.7
^{115}In	28.3	20.6	7.7
^{116}Sn	28.2	20.7	7.5
^{116}Sn	28.1	20.7	7.4

[a] Reference 33.

proton distribution. Although this conclusion agrees with results of previous optical-model studies,[31] it contrasts with that of a recent study by Auerbach *et al.*,[35] who conclude, surprisingly, that the neutron radius for ^{208}Pb is perhaps somewhat smaller than the proton radius.

Owing to the relative constancy of RMSR and its dependence on both the diffuseness a and the radius r_0, the choice of a particular value for r_0 defines a corresponding value for a, and vice versa. Moreover, once r_0 is defined the depth V is no longer ambiguous (except for the discrete ambiguity between families). So all these parameters are more or less defined once one of them is defined. Thus, variation of all of them in the fitting routine results in ambiguities arising from the insensitivity of the scattering to the precise shape of the potential, and holding one of them fixed removes most of these ambiguities. We chose to fix the radius parameter r_0 because of, perhaps, a better intuitive understanding about nuclear sizes and a longer history of the study of nuclear sizes. We chose the value $r_0=$ 1.24 F for several reasons: This value is within the broad range of values that give equally good fits, it corresponds to a value for a that is consistent with values from nucleon scattering studies and is slightly greater than the value of about 0.5 F found from electron scattering studies, and it is approximately equal to values used previously in proton, neutron, deuteron, and triton investigations.[36,37] Nevertheless, recent studies suggest that a somewhat smaller value may be preferred.[38]

Accordingly, with r_0 fixed at 1.24 F, five-parameter searches (varying V, a, W, r_0', and a', with $V_{so}=0$) were performed on all the angular distributions with V set initially at 150 MeV. The fits to the data that these searches produced are shown in Figs. 1–4. It can be seen that these fits without spin orbit, represented by the solid lines in the figures, are relatively poor in the back-angle regions for ^{51}V, ^{59}Co, and ^{60}Ni. In an attempt to improve the fits in the back-angle region for these cases, six parameter searches (letting V_{so} vary too) were performed. The resulting fits are represented by the dashed lines in Figs. 1, 2, and 4. It is quite evident in these cases that *the inclusion of the spin-orbit potential substantially improves the fits.*

No attempt was made to include the spin-orbit term to fit the angular distributions of ^{89}Y, ^{90}Zr, ^{114}Cd, ^{115}In, and ^{116}Sn because good fits were obtained without it.

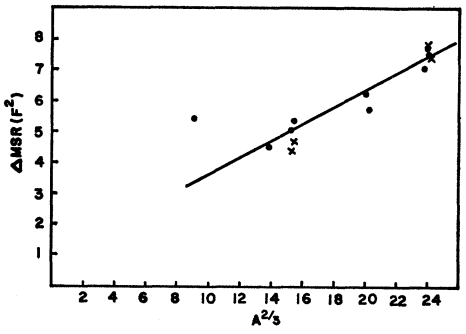

FIG. 9. Difference between the mean-square ^{3}He radius and the mean-square electron radius versus the atomic mass of the target. Values of ΔMSR are from Table III. The dots (·) are the values for the 30-MeV data, and the crosses (×) are the values for 35-MeV data. The straight line has been drawn to show approximately the average dependence on $A^{2/3}$.

There appear to be three distinct types of angular distributions: those for ^{51}V, ^{59}Co, and ^{60}Ni, where the back-angle undulations are strong and the spin-orbit potential is required for good fits, those for ^{89}Y and ^{90}Zr, where the back-angle undulations are also strong but the spin-orbit potential is not required for good fits, and those for ^{114}Cd, ^{115}In, and ^{116}Sn, where there are virtually no back-angle undulations and, of course, the spin-orbit potential is not required for good fits. The situation for ^{27}Al seems to be special and will be discussed separately.

The 150-MeV families of parameters that produce the fits shown in Figs. 1–4 are listed in Table IV. These parameters agree in general with those obtained in previous studies, except that here some spin-orbit values are included.[39]

As is evident in Figs. 1, 2, and 4, the major effect of the spin-orbit interaction is to damp the back-angle undulations. In general, whenever the spin-orbit potential is required for a good fit, the amplitude for the back-angle undulations calculated without the spin-orbit potential included is greater than the observed amplitude, and the damping effect of the spin-orbit potential is necessary to bring the calculated amplitude into agreement with the measured amplitude. Thus, our results seem to indicate that in certain cases the effect of the spin-orbit potential is readily apparent in elastic scattering data.

Moreover, the resulting magnitudes for the spin-orbit potential are roughly consistent with theoretical expectations. In particular, the value of $V_{so}=2.4$ MeV for ^{60}Ni at 35 MeV is in excellent agreement with the

[35] E. H. Auerbach, H. M. Qureshi, and M. M. Sternheim, Phys. Rev. Letters **21**, 162 (1968); see also H. A. Bethe and P. J. Siemens, Phys. Letters **27B**, 549 (1968).

[36] R. L. Cassola and R. D. Koshel, Nuovo Cimento **55B**, 83 (1968); **53B**, 363 (1968); C. M. Perey and F. G. Perey, Phys. Letters **26B**, 123 (1968); J. C. Hafele, E. Flynn, and A. G. Blair, Phys. Rev. **155**, 1238 (1967); L. Rosen, J. G. Beery, A. S. Goldhaber, and E. H. Auerbach, Ann. Phys. (N.Y.) **34**, 96 (1965); and Ref. 37.

[37] C. M. Perey and F. G. Perey, Phys. Rev. **132**, 755 (1963).

[38] M. P. Fricke and G. R. Satchler, Phys. Rev. **139**, B567 (1965); P. G. Roos and N. S. Wall, *ibid.* **140**, B1237 (1965); and Ref. 3.

[39] The predicted values for the total reaction cross sections σ_r are also listed in Tables IV and V. Though measured values for σ_r are scarce, a recent paper [R. Balcarcel and J. A. R. Griffith, Phys. Letters **26B**, 213 (1968)] reports a measurement of $\sigma_r=$ 1.70±0.03 b for 28.7-MeV ^{3}He incident on Ni. While the agreement of our predicted value of 1.59 b (for 29.5-MeV ^{3}He incident on ^{60}Ni) with this measured value is not particularly satisfying, it represents a considerable improvement over the prediction quoted by Balcarcel and Griffith.

TABLE IV. Families of parameters that produce minimum χ^2 fits to the experimental cross sections. For all these cases the real radius parameter was held fixed at $r_0 = 1.24$ F.

Energy (MeV)	Element	Family	V (MeV)	a (F)	W (MeV)	r_0' (F)	a' (F)	V_{so}[a] (MeV)	σ_r[b] (b)	χ^2
29.6	^{51}V	*a*	53.8	0.461	13.4	1.41	1.18	1.6	1.64	13.3
		b	85.1	0.464	15.3	1.44	1.16	2.8	1.73	10.7
		c	112.8	0.693	15.6	1.59	0.903	3.1	1.64	4.7
		d	156.4	0.580	20.8	1.44	1.03	3.8	1.72	4.3
		d−1	158.1	0.560	24.5	1.35	1.07	···	1.71	7.6
		e	204.6	0.545	25.9	1.36	1.10	4.0	1.79	5.0
29.5	^{59}Co	*a*	54.3	0.513	15.7	1.36	1.18	3.2	1.67	7.2
		b	85.5	0.523	23.1	1.29	1.18	3.5	1.77	5.7
		c	110.3	0.713	15.1	1.65	0.817	4.3	1.66	1.3
		d	150.7	0.656	20.1	1.54	0.906	5.1	1.72	1.7
		d−1	153.2	0.643	29.5	1.41	0.945	···	1.72	2.9
		e	196.6	0.622	28.1	1.40	0.976	5.4	1.74	2.3
29.5	^{60}Ni	*a*	55.2	0.494	18.3	1.35	1.17	1.9	1.69	5.5
		b	85.6	0.483	20.5	1.33	1.2	3.6	1.77	5.3
		c	109.5	0.706	15.2	1.63	0.807	4.1	1.62	2.4
		d	149.6	0.665	19.0	1.54	0.854	4.9	1.59	1.6
		d−1	150.9	0.663	25.8	1.46	0.845	···	1.58	5.0
		e	194.6	0.625	25.8	1.42	0.944	5.7	1.69	2.9
29.6	^{89}Y	*a*	45.7	0.576	15.4	1.26	1.20	···	1.58	5.0
		b	90.2	0.725	16.7	1.48	0.714	···	1.43	3.6
		c	122.6	0.530	15.1	1.53	1.03	···	1.83	1.8
		d	149.8	0.651	18.5	1.54	0.891	···	1.77	1.6
		e	186.0	0.629	22.1	1.46	0.931	···	1.76	1.8
29.6	^{90}Zr	*a*	45.9	0.677	17.6	1.29	0.937	···	1.32	12.1
		b	88.7	0.737	16.6	1.50	0.697	···	1.42	3.2
		c	123.6	0.571	22.5	1.27	1.13	···	1.67	2.0
		d	154.0	0.587	21.6	1.38	1.04	···	1.73	1.6
		e	190.7	0.527	17.7	1.55	1.03	···	1.93	2.5
29.7	^{114}Cd	*a*	49.6	0.794	16.6	1.42	0.806	···	1.41	1.0
		b	87.9	0.716	25.3	1.32	0.840	···	1.44	1.1
		c	120.3	0.677	29.6	1.26	0.887	···	1.47	1.4
		d	146.0	0.652	32.0	1.19	0.927	···	1.46	1.5
		e	180.4	0.638	38.7	1.14	0.942	···	1.49	1.8

TABLE IV. (*Continued*).

Energy (MeV)	Element	Family	V (MeV)	a (F)	W (MeV)	r_0' (F)	a' (F)	V_{so}[a] (MeV)	σ_r[b] (b)	χ^2
29.8	^{115}In	*a*	57.4	0.826	20.2	1.47	0.724	···	1.45	0.9
		b	89.8	0.747	23.6	1.42	0.727	···	1.44	0.8
		c	121.1	0.709	25.2	1.41	0.750	···	1.48	0.9
		d	150.5	0.661	22.8	1.41	0.891	···	1.64	0.6
		e	180.2	0.636	36.9	1.21	0.783	···	1.37	2.5
29.5	^{116}Sn	*a*	47.8	0.852	10.6	1.61	0.653	···	1.41	0.8
		b	91.4	0.744	14.6	1.56	0.712	···	1.48	0.5
		c	118.1	0.708	17.4	1.51	0.728	···	1.48	0.5
		d	149.9	0.673	21.4	1.46	0.756	···	1.48	0.5
		e	183.3	0.652	23.9	1.43	0.781	···	1.50	0.5
34.8	^{59}Co	*a*	52.8	0.464	15.0	1.43	1.20	2.8	1.82	11.0
		b	81.9	0.459	19.9	1.39	1.20	2.9	1.93	10.1
		c	111.3	0.682	17.9	1.58	0.899	4.3	1.78	2.8
		d	152.8	0.628	23.7	1.46	0.994	5.4	1.84	3.3
		d−1	156.4	0.625	32.3	1.36	1.01	···	1.85	5.4
		e	199.5	0.600	33.0	1.31	1.06	6.2	1.87	4.2
35.1	^{60}Ni	*a*	51.1	0.509	14.9	1.46	1.08	1.7	1.71	12.0
		b	73.1	0.733	13.0	1.70	0.781	1.8	1.70	3.8
		c	110.6	0.664	18.4	1.57	0.871	2.2	1.74	3.4
		d	150.6	0.621	22.9	1.50	0.938	2.4	1.80	4.0
		d−1	149.5	0.635	24.8	1.49	0.928	···	1.80	4.3
		e	194.6	0.605	30.1	1.40	0.976	1.3	1.82	5.5
35.3	^{115}In	*a*	65.4	0.824	13.0	1.60	0.713	···	1.72	2.0
		b	91.6	0.761	17.8	1.52	0.762	···	1.75	1.9
		c	114.8	0.718	23.6	1.47	0.850	···	1.88	1.3
		d	147.3	0.685	24.2	1.45	0.873	···	1.89	1.4
		e	179.7	0.676	24.9	1.46	0.872	···	1.92	1.9
35.2	^{116}Sn	*a*	63.5	0.793	13.1	1.60	0.759	···	1.77	1.8
		b	90.3	0.733	16.3	1.54	0.811	···	1.79	2.3
		c	111.4	0.747	18.5	1.55	0.771	···	1.80	2.8
		d	148.9	0.668	26.1	1.40	0.877	···	1.78	3.0
		e	176.2	0.671	32.8	1.38	0.843	···	1.78	2.8

[a] Where there is no entry for V_{so}, the spin-orbit potential was not included in the fit.

[b] Values for the total reaction cross section calculated by the optical-model computer code.

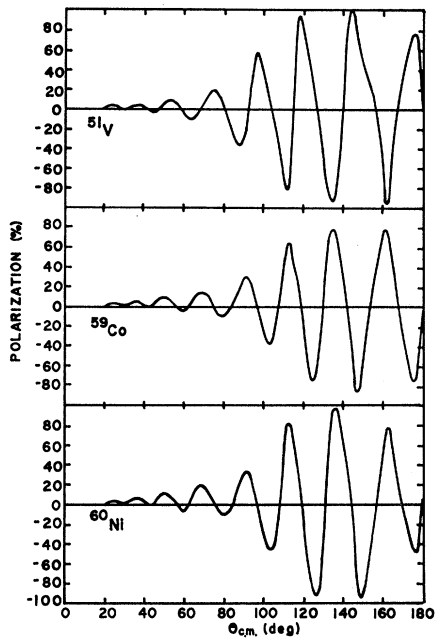

FIG. 10. Predicted polarizations of 30-MeV ^{3}He projectiles elastically scattered from ^{51}V, ^{59}Co, and ^{60}Ni. The potential parameters that produce these polarizations are listed in Table IV, families *d*.

expected range of 2–3 MeV. For ^{60}Ni at 30 MeV, however, $V_{so}=4.9$ MeV, a value that is somewhat larger than is expected. Furthermore, such a large variation in V_{so} from 30–35 MeV is inconsistent with the basic philosophy of the optical model, that is, a slow and smooth dependence of the potential parameters on the projectile energy and the target mass. Perhaps a partial explanation for this difference can be found in one of our experimental difficulties. At forward angles the elastic yields were recorded with the targets in transmission, but at back angles it was necessary to record with the targets in reflection, a geometry that causes an additional spread in the energy resolution and, in the case of ^{60}Ni, caused a considerable overlapping of the elastic peak with the peak for the first excited state. Though the elastic and inelastic peaks were always recognizable, the subtraction of the overlapping inelastic yield may have been fairly imprecise in some cases. The result of such an error, of course, is likely to be an artificial damping of the back-angle undulations, and the greater the damping the greater the value of V_{so} required to produce a good fit. Since this problem was more serious at 30 than at 35 MeV, it may at least partially explain the greater value for V_{so} at 30 MeV. We hope to repeat this experiment with better resolution and thereby resolve this question.

In any event, no such experimental problems arose in the case of ^{59}Co, where the values of V_{so} at both 30 MeV ($V_{so}=5.1$ MeV) and 35 MeV ($V_{so}=5.4$ MeV) are similar and consistently higher than expected theoretically. Furthermore, and more importantly, these values are consistently higher than the corresponding values for ^{60}Ni, another difference that is against the basic philosophy of the optical model. A difference of 1 amu in these two cases should result in a negligible difference in the depth of the spin-orbit potential. Perhaps the fact that ^{59}Co is an odd-A nucleus while ^{60}Ni is even causes an observable difference in the back-angle scattering.

In general, the target spin-orbit interaction for odd-A nuclei is expected to damp the back-angle undulations,[16] a characteristic identical with the ordinary projectile spin-orbit interaction. Therefore, the unexpectedly large values of V_{so} for ^{51}V and ^{59}Co and particularly the large value for ^{59}Co compared to ^{60}Ni at 35 MeV suggest that target spin effects may be evident in back-angle elastic scattering. However, before any definitive conclusions can be drawn, a more accurate and systematic study of these back-angle cross sections is desired.

Of course, polarization data would certainly help in choosing more precise strengths for the spin-orbit potentials. Polarizations predicted from the spin-orbit depths found in this investigation are shown in Figs. 10 and 11 and may be useful in future polarization experiments.

The parameters obtained for the 150-MeV family for ^{27}Al are listed in Table V. In this case only relatively poor fits were obtained with $r_0=1.24$ F, so seven-parameter searches (letting r_0 vary too) were performed. As can be seen in Fig. 2, the resulting fits are respectable, particularly with the spin-orbit potential included, but the resulting values for the parameters are not at all similar to those found for the other targets. Such great differences as these again are incompatible with the basic philosophy of the optical model. Perhaps data for neighboring nuclei having both zero and nonzero spin would help to clarify the situation; it may be that the

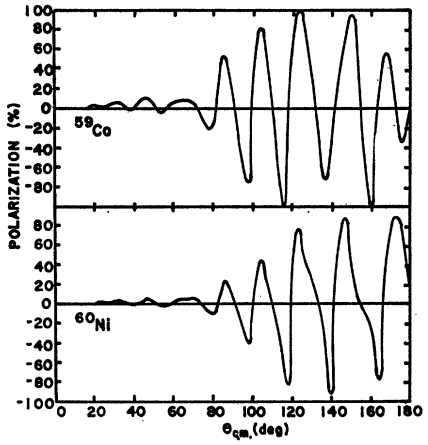

FIG. 11. Predicted polarizations of 35-MeV ^{3}He projectiles elastically scattered from ^{59}Co and ^{60}Ni. The potential parameters that produce these polarizations are listed in Table IV, families *d*.

TABLE V. Families of parameters that give minimum χ^2 fits to the ^{27}Al data. The incident energy for this case was 29.6 MeV.

Family	V (MeV)	r_0 (F)	a (F)	W (MeV)	r_0' (F)	a' (F)	V_{so}[a] (MeV)	σ_r (b)	χ^2
a	67.1	1.39	0.690	13.6	1.77	0.785	6.9	1.41	5.3
b	104.2	1.43	0.593	28.1	1.35	0.976	10.3	1.50	6.0
c	163.2	1.37	0.560	35.8	1.21	1.06	12.7	1.51	7.3
$c-1$	178.3	1.38	0.526	81.4	0.743	1.20	...	1.53	23.7
d	219.6	1.36	0.544	80.0	0.706	1.20	16.7	1.51	10.5

[a] Where there is no entry for V_{so}, the spin-orbit potential was not included in the fit.

nuclear spin of ^{27}Al plays a significant role. Moreover, the validity of the optical-model philosophy for such a light nucleus as ^{27}Al may be questionable.

The existence of families of parameters that have different real well depths and that produce comparable fits to the data represents a discrete ambiguity of the optical potential. A discrete jump in the real depth for these families corresponds to an additional half-wavelength of each partial wave in the interior of the optical potential and to very little difference at the edge of the potential.[37] Since the calculated cross section depends primarily on the wave function at the nuclear surface and is highly insensitive to details of the wave function in the interior region,[37] the fits produced by the different families are nearly indistinguishable. From a strictly theoretical point of view, however, only the families with a real depth of about 150 MeV are interesting. Nevertheless, it seems desirable from an experimental point of view to look for indications in the data that the 150-MeV family is indeed the "correct" one, for there may be fine effects that depend to a certain extent on the interior wave function.

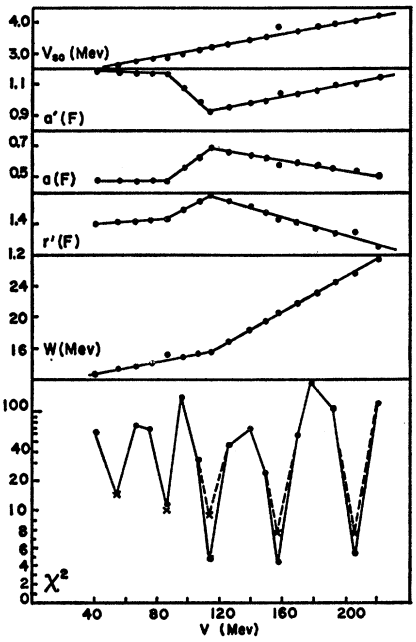

FIG. 12. Parameter families with and without the spin-orbit potential included for 30-MeV ^{3}He projectiles elastically scattered from ^{51}V. The values of χ^2 obtained without the spin-orbit potential are denoted by crosses (×) and the values obtained with the spin-orbit potential are denoted by dots (·). The value of r_0 was held fixed at 1.24 F.

Therefore, the different families of parameters with a real depth between about 50 and 200 MeV were found by performing five-parameter searches for each angular distribution (six-parameter searches with $V_{so}\neq 0$ for ^{51}V, ^{59}Co, and ^{60}Ni) with starting values for V of about 50, 80, 110, and 200 MeV. For reasons already discussed above in connection with the 150-MeV families, the radius parameter r_0 was held fixed at 1.24 F. All the resulting parameter families are listed in Table IV. The parameter families resulting from similar searches for ^{27}Al are included in Table V. As was the case for the 150-MeV families for ^{27}Al, it was necessary to allow variation of r_0 to get acceptable fits.

Our experience has been that a χ^2 value of the order of 1 represents a fit that is visually good. Furthermore, an increase in the value of χ^2 of about a factor of 2 is required before there is a discernible deterioration in the visual quality of the fit.[40] Thus, if a factor-of-2 increase is taken as the basis for a relatively poor fit, a study of the χ^2 values in Tables IV and V shows that the different families for ^{27}Al, ^{114}Cd, ^{115}In, and ^{116}Sn give equally good fits, and there is no observational preference for one over the others. However, for the other cases, and particularly for ^{51}V, ^{59}Co, and ^{60}Ni, where the spin-orbit potential is required, there are significant differences in the χ^2 values for the different families. For these cases the 50- and 80-MeV families can be

[40] The value of χ^2 alone is not always a foolproof criterion for choosing the actual best fit. Indeed, it is possible in some cases that a larger value for χ^2 actually corresponds to a better fit [J. Högaasen, Nuovo Cimento **55B**, 595 (1968)]. The possibility of a diabolical inversion of the correspondence between the smallest value of χ^2 and the best fit was guarded against by always visually checking the fits.

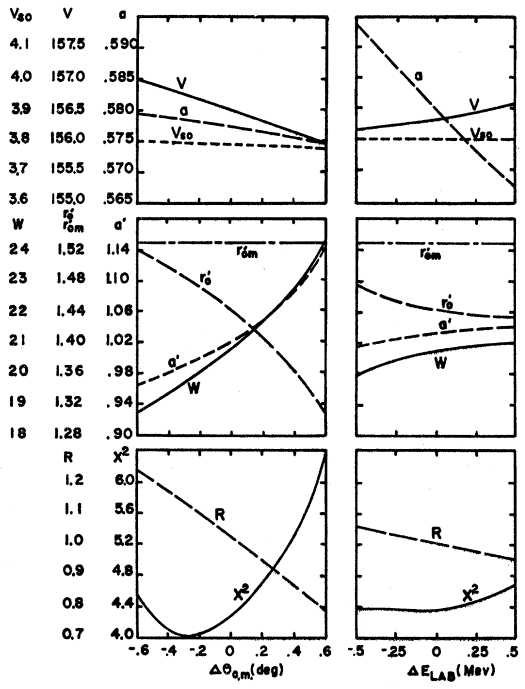

FIG. 13. Dependence of the best-fit parameters on systematic errors in the detector angle θ and the beam energy E for 30-MeV ^{3}He projectiles scattered from ^{51}V. The real radius parameter r_0 was held fixed at 1.24 F. The dependence of r_{0m}', the imaginary root-mean-square radius divided by $A^{1/3}$, is also shown.

excluded for their production of relatively poor fits. Though the 200-MeV families produce better fits and cannot be definitely excluded, the 100- and 150-MeV families produce comparable and definitely superior fits. Thus, it seems that there is a purely observational basis for preferring the families of parameters with a real depth of either 100 or 150 MeV. It must be that strong back-angle undulations in the elastic cross section depend to a certain extent on the details of the interior wave function. Further studies in this area are clearly indicated.

The case of ^{51}V was chosen for a more detailed investigation of the role of the spin-orbit potential in this question of a preferred family of parameters. The parameters for each family obtained with the spin-orbit potential included and the corresponding values for χ^2 are plotted as dots versus the real depth in Fig. 12. Since the parameters for the different families were found to change systematically, parameter values intermediate to those for the families were chosen and found to produce the corresponding intermediate values for χ^2 shown in Fig. 12. It can be seen that the χ^2 values corresponding to $V=54$, 85, 113, 156, and 205 MeV represent definite local minima in the χ^2 space, and that the 113- and 156-MeV families produce the best fits. In order to determine the extent to which the inclusion of the spin-orbit potential improves the fits, five-parameter searches with $V_{so}=0$ were also performed for each family. The resulting values of χ^2 for each of the families with $V_{so}=0$ are plotted as crosses in Fig. 12. A comparison of these two values of χ^2 for each of the families shows that the quality of the fits for the 54- and 85-MeV families is not improved by the inclusion of the spin-orbit potential. On the other hand, the fits for the 113-, 156- and 205-MeV families are substantially improved by the inclusion of the spin-orbit potential (the χ^2 scale in Fig. 12 is linear from 0–10 and logarithmic from 10–100). This strong indication of preferred families when the spin-orbit potential is included is similar to the results of a study of deuteron scattering,[14] where it was found that the 100-MeV family is preferred when a spin-orbit potential is included. Perhaps more extensive back-angle data would go even further and provide an observational preference between the 113- and 156-MeV families.

Finally, uncertainties in the values of the best-fit parameters arising from imprecision of the data should not be ignored in optical-model analysis. Figure 13 shows the results of an investigation of the dependence of the 150-MeV family of parameters for the ^{51}V data on systematic shifts in the detector angle θ and the beam energy E (the measured energy in this case was 29.6 MeV $\pm 1\%$). This investigation of the effects of a systematic error in θ or E was carried out so as to duplicate the procedure that would have been used had there been an (unknown) systematic error in θ or E. Thus, for example, all the values of θ in the data were changed to $\theta+\Delta\theta$, and these new data were treated as though they were the original data. Because the original angular distributions were always first renormalized for optimum forward-angle agreement before searching for best-fit parameters, these new angular distributions were also renormalized in the same way before searching for new best-fit parameters. It should be mentioned that this approach was not used in previous studies of this type.[18]

If $R\sigma$ is the renormalized measured cross section and σ_{Ruth} is the Rutherford cross section, the renormalization procedure forces the equality $R\sigma=\sigma_{\text{Ruth}}$ for $\theta \ll 1$. Since the measured cross section is inversely proportional to the effective target thickness T and the integrated current Q, $\sigma \propto 1/TQ$, and since $\sigma_{\text{Ruth}} \propto 1/E^2\theta^4$ for small θ, the renormalization produces a value for $R \propto TQ/E^2\theta^4$. If there were no error in E, θ, T, or Q, the value for R would be 1, but systematic errors in these quantities produce deviations from unity:

$$\Delta R=(\Delta T/T)+(\Delta Q/Q)-2(\Delta E/E)-4(\Delta\theta/\theta).$$

Figure 13 shows that R obtained in the standard way has a strong dependence on $\Delta\theta$ and a somewhat weaker dependence on ΔE, just as is expected from the above relationship. Owing to this rather strong dependence on $\Delta\theta$, it is not at all surprising that elastic cross sections for charged projectiles nearly always require a certain

renormalization for forward-angle agreement, particularly if extraordinary attention has not been given to elimination of systematic errors in the detector angles. Figure 13 shows that our estimated angular error of $\pm 0.1°$ corresponds to a renormalization of as much as $\pm 4\%$. When, in addition, our energy uncertainty of $\pm 1\%$, target thickness uncertainty of $\pm 5\%$, and current integration uncertainty of $\pm 1\%$ are taken into account, renormalization factors as large as 12% (0.88–1.12) can be expected. The values of R actually required for each angular distribution in all cases differed from unity by less than this expected maximum deviation.

Further examination of Fig. 13 shows that, even with renormalization after each change, some of the parameters still have a strong dependence on either the energy error or the angular error. It can be seen that the real diffuseness a is particularly sensitive to energy error, and the imaginary-well parameters W, r_0', and a' are very sensitive to angular error. However, the spin-orbit depth V_{so} seems to be fairly insensitive to either energy or angular error. Moreover, it appears that another quantity is insensitive to these errors: the root-mean-square radius for the imaginary well (RMSR'). Much as the value of RMSR for the real well is independent of the particular values of r_0 and a, the value of RMSR', which is plotted in Fig. 13 as $r_{0m}' = \text{RMSR}'/A^{1/3}$, seems to be independent of the particular values of r_0' and a'. The physical meaning of the imaginary-well root-mean-square radius is not entirely clear; perhaps it represents an average breakup radius for the incident ^{3}He projectiles. Whatever it means, this quantity appears to be fairly uniquely defined by an optical-model analysis.

Let us assume that RMSR' is uniquely defined by an optical-model analysis, that it represents the most probable radius for absorption, and that the most probable point for absorption of compound projectiles is at the nuclear surface. If these assumptions are correct, there should be a more systematic and smooth variation of RMSR' with A than there is for the individual imaginary geometrical parameters, which are likely to be subject to considerable ambiguity. Furthermore, there should exist a definite relationship between the most probable absorption radius RMSR' and the nuclear radius, which to a fair approximation can be represented unambiguously by 1.29 RMSR.[41]

[41] RMSR for a Woods-Saxon well is given by the formula in Ref. 32. In the limit of a vanishingly small ratio of diffuseness to radius parameters, $a/\mathcal{R} \to 0$, the Woods-Saxon well becomes a square well of radius $\mathcal{R}$, and $\text{RMSR} = (\frac{3}{5})^{1/2}\mathcal{R}$. Thus, the radius $\mathcal{R}$ of a square well with the same RMSR as a corresponding Woods-Saxon well is given by $\mathcal{R} = (5/3)^{1/2}\text{RMSR} = 1.29$ RMSR. Therefore, 1.29 RMSR represents a unique first approximation for the radius of the nuclear surface if the real diffuseness is small. Moreover, if the imaginary diffuseness is small, for a Woods-Saxon (volume) imaginary potential $\text{RMSR}' \cong (\frac{3}{5})^{1/2}\mathcal{R}'$, and for a derivative Woods-Saxon (surface-peaked) imaginary potential $\text{RMSR}' \cong \mathcal{R}'$, where $\mathcal{R}'$ is the imaginary-well radius parameter (Ref. 1, p. 191).

TABLE VI. Root-mean-square radii for real and imaginary wells. The column labeled RMSR lists the square roots of the values of Table III, and the column labeled RMSR' lists imaginary-well root-mean-square radii derived from the relation of Ref. 32 and the imaginary parameters of the 150-MeV families of Tables IV and V (parameters from the families with the spin-orbit potential were used in those cases where it was included). The third column lists the differences and the last column lists the ratios. Radii derived from the results of the 30- and 35-MeV data are grouped separately. All radii are in Fermis.

Nucleus	RMSR	RMSR'	RMSR'-RMSR	RMSR'[a]/RMSR
		30-MeV data		
^{27}Al	3.81	4.83	1.02	1.28
^{51}V	4.16	5.64	1.48	1.36
^{59}Co	4.45	5.76	1.31	1.29
^{60}Ni	4.49	5.65	1.16	1.26
^{89}Y	4.92	6.25	1.33	1.27
^{90}Zr	4.84	6.14	1.30	1.27
^{114}Cd	5.24	5.05[b]	...	...
^{115}In	5.32	6.28	0.96	1.18
^{116}Sn	5.31	6.15	0.84	1.16
		35-MeV data		
^{59}Co	4.37	5.76	1.39	1.32
^{60}Ni	4.42	5.72	1.30	1.29
^{115}In	5.32	6.37	1.05	1.20
^{116}Sn	5.30	6.24	0.94	1.18

[a] This ratio should approach 1.29 in the limit of small diffuseness parameters if the average absorption radius equals the average nuclear radius (see the text for details).

[b] This very low value for ^{114}Cd is inconsistent with the quite smooth dependence of the other cases on the atomic mass of the corresponding nucleus, and on this basis it will be excluded from further consideration.

These assumptions are in agreement with previous observations that equally good fits to compound projectile data can be obtained with either volume or surface-peaked imaginary potentials, with the result that the volume imaginary radius parameter is consistently larger than the corresponding surface-peaked imaginary radius parameter.[37] Because RMSR' for a volume Woods-Saxon potential is less than the radius parameter, the choice of volume absorption results in an imaginary radius parameter that is greater than the real radius parameter. On the other hand, because RMSR' for a derivative Woods-Saxon potential approximately equals the radius parameter,[41] the choice of surface-peaked absorption results in an imaginary radius parameter that approximately equals the real radius parameter. The point is that, regardless of the choice of the form of the potential, the analysis adjusts the parameters so that RMSR' remains the same.

These ideas seem to be partially verified by the values of RMSR and RMSR′ listed in Table VI. The radii listed in Table VI were derived from the parameters for the 150-MeV families of Tables IV and V. This table shows that the differences between RMSR′ and RMSR are roughly constant at about 1.2 F and that the ratios agree surprisingly well with the expected value of about 1.29.

V. SUMMARY

Although our study seems to have answered some questions, it has left others unanswered and has suggested new ones. We have learned little that is new for the heavy nuclei ^{114}Cd, ^{115}In, and ^{116}Sn. For the nuclei ^{89}Y and ^{90}Zr, our results suggest that back-angle data suppresses somewhat the number of parameter families that produce equally good fits. Our results for ^{27}Al are anomalous; reasonably good fits are obtained only with parameters that bear little resemblance to average values for the other cases.

On the other hand, our results for the nuclei ^{51}V, ^{59}Co, and ^{60}Ni are considerably more interesting. In some cases they are definitive and in others highly heuristic: (1) Back-angle elastic data for these nuclei reflect the effect of the spin-orbit interaction as an otherwise unexplained suppression of the back-angle undulations; (2) the required spin-orbit strength is fairly consistent with an inverse dependence on the mass of the projectile; (3) inclusion of the spin-orbit interaction significantly reduces the ambiguity between families of parameters; and (4) target spin effects seem to be apparent in back-angle elastic data. These results indicate that, in order to achieve a better understanding of the relatively simple process of elastic scattering, a careful, systematic, back-angle study of neighboring even-odd-even triplets of nuclei in this region is highly desirable.

ACKNOWLEDGMENTS

We are grateful to the entire Cyclotron staff for their dedication to the production of suitable ^{3}He beams, to R. Mewaldt and G. Siegel for helping with the long hours of operation of the Cyclotron, and to G. Kretschmann, E. Minder, and R. Head for their assistance with the construction of the scattering chamber. We are especially thankful for the extensive computer time provided by the Washington University Computing Services.